

See discussions, stats, and author profiles for this publication at: <https://www.researchgate.net/publication/228727133>

Wafer-Scale Surface-Enhanced Raman Scattering Substrates with Highly Reproducible Enhancement

ARTICLE *in* THE JOURNAL OF PHYSICAL CHEMISTRY C · AUGUST 2009

Impact Factor: 4.77 · DOI: 10.1021/jp905065z

CITATIONS

36

READS

33

5 AUTHORS, INCLUDING:



Bin Jiang

Hangzhou Dianzi University

567 PUBLICATIONS 6,581 CITATIONS

SEE PROFILE

Wafer-Scale Surface-Enhanced Raman Scattering Substrates with Highly Reproducible Enhancement

Xuefeng Liu,^{*,†} Chih-Hung Sun,[‡] Nicholas C. Linn,[‡] Bin Jiang,[§] and Peng Jiang^{*,‡}

School of Chemical and Material Engineering, Jiangnan University, Wuxi, Jiangsu 214122, China, Department of Chemical Engineering, University of Florida, Gainesville, Florida 32611, and Department of Mathematics and Statistics, Portland State University, Portland, Oregon 97201

Received: May 29, 2009; Revised Manuscript Received: June 30, 2009

Here, we report a simple colloidal templating approach for fabricating surface-enhanced Raman scattering (SERS) substrates with highly reproducible enhancement over wafer-sized areas. The substrates are produced by evaporating a thin layer of gold on highly ordered silica colloidal crystal–polymer nanocomposites created by a scalable spin-coating technology. The ordered inorganic–organic composite structure induces the formation of island-type gold films. Systematic measurements and statistical analysis show that the substrates exhibit high SERS reproducibility with less than 28% standard deviation over a 4 in. wafer surface. Finite element electromagnetic modeling has also been employed to simulate SERS enhancement from these structured substrates.

Introduction

Surface-enhanced Raman scattering (SERS) has attracted resurging interest because of significant advances in new synthetic and nanofabrication methodologies for creating well-defined nanoparticles and nanostructures as well as its great potential for developing ultrasensitive chemical and biological sensors for a wide spectrum of applications, ranging from detection of chemical warfare agents to environmental monitoring.^{1–14} Aggregated nanoparticles of noble metals (e.g., Au and Ag) have been demonstrated to allow the detection of single molecules.^{15,16} A recent systematic study shows that relatively low SERS enhancement factors (as low as 10^7) are sufficient for enabling single-molecule detection.¹⁷ Unfortunately, the nanoparticle aggregation process is usually stochastic, and the distribution of the electromagnetic “hot spots”, which contribute most to the overall SERS intensity, is random.⁴ This results in terribly poor reproducibility of SERS enhancement and has greatly hampered the practical applications of SERS techniques. The reproducibility issue also haunts another type of widely exploited SERS substrates, the electrochemically roughened metal surfaces, which exhibit a SERS enhancement factor of 10^4 – 10^5 .^{18–22} It is not uncommon to observe SERS intensity variation by a factor of 10 or higher across a centimeter-sized sample surface. To resolve this formidable challenge, various painstaking top-down nanolithography technologies, such as electron beam lithography and focused ion beam have been utilized to create SERS-active nanostructures with arbitrary geometries.^{23,24} However, achieving high-throughput and inexpensive nanofabrication over large areas is still challenging for these top-down techniques.

Bottom-up colloidal self-assembly and templating nanofabrication have been broadly employed as an inexpensive and simple-to-implement alternative to nanolithography in creating periodically structured SERS substrates.^{25–30} Nanosphere li-

thography (NSL), which uses monolayer or double-layer colloidal crystals as either a deposition or etching mask to define periodic mosaic arrays of microcolumnar structures inside the voids of colloids, has been demonstrated as a viable technology for generating SERS-active substrates.³¹ The periodic surface of self-assembled colloidal monolayers has also been used as a structural template to fabricate the so-called metal film over nanosphere (MFON) for a large variety of applications ranging from electrochemical SERS to fundamental studies of SERS mechanisms.^{27,32} Electrochemical deposition of metals and evaporation-induced assembly of nanoparticles in the interstitial voids of three-dimensional ordered colloidal crystals have also been developed to yield structured SERS substrates.^{26,28} Bartlett et al. have shown that sculpted nanovoid arrays exhibit high SERS reproducibility with standard deviation of less than 12.5% across a centimeter-sized surface.²⁵ Unfortunately, current colloidal self-assembly technologies suffer from several drawbacks. First, it usually takes days or even weeks to assemble a centimeter-sized sample. Second, most of the available bottom-up techniques are not compatible with standard microfabrication, limiting the throughput and on-chip integration of practical devices. Third, only limited, close-packed crystalline structures are available through conventional colloidal self-assembly.

We have recently developed a scalable and microfabrication-compatible spin-coating technology for assembling wafer-sized colloidal crystals with remarkably large single-crystalline domains and unusual nonclosed-packed structures.^{33,34} Using spin-coated monolayer colloidal crystals as templates, we have fabricated periodic gold nanopillar arrays with nanoscale sharp tips.³⁵ They have also been demonstrated as SERS-active substrates with a high enhancement factor (up to 10^8).^{36,37} However, the fabrication process involves multiple steps (e.g., metal deposition, mask liftoff, and KOH anisotropic etch), and each step could introduce some defects and uncertainties. The accumulation of defects results in poor reproducibility and large variation (>100%) in SERS enhancement over wafer-scale areas. Here, we report a much simpler templating technology that only requires a single metal deposition step for creating SERS substrates with high reproducibility over large areas. The new

* Corresponding authors. E-mail: pjiang@che.ufl.edu; xfliu@jiangnan.edu.cn.

† Jiangnan University.

‡ University of Florida.

§ Portland State University.

methodology leverages the high uniformity of the spin-coated colloidal arrays and well-established physical vapor deposition techniques.

Experimental Section

Materials and Substrates. All solvents and chemicals are of reagent quality and are used without further purification. Monodispersed silica spheres with 320 and 400 nm diameters and less than 5% diameter standard deviation are synthesized by the Stöber method.³⁸ Ethoxylated trimethylolpropane triacrylate (ETPTA) monomer is obtained from Sartomer (Exton, PA). The photoinitiator, Darocur 1173 (2-hydroxy-2-methyl-1-phenyl-1-propanone), is provided by Ciba Specialty Chemicals. The (3-acryloxypropyl)trichlorosilane (APTCS) is purchased from Gelest. Silicon wafers [test grade, n-type, (100)] are obtained from Wafernet and are primed by swabbing APTCS on the wafer surfaces using cleanroom Q-tips (Fisher), rinsed and wiped with 200 proof ethanol 3 times, spin coated with a 200 proof ethanol rinse at 3000 rpm for 1 min, and baked on a hot plate at 110 °C for 2 min. Benzenethiol (>98% purity) is purchased from Sigma-Aldrich. Pure chromium and gold pellets are obtained from Kurt J. Lesker.

Instrumentation. Scanning electron microscopy (SEM) is carried out on a JEOL 6335F FEG-SEM. Atomic force microscopy (AFM) is performed on a Digital Instruments Dimension 3100 unit. A WS-400B-6NPP-Lite spin processor (Laurell) is used to spin-coat colloidal suspensions. The polymerization of an ETPTA monomer is carried out on a pulsed UV curing system (RC 742, Xenon). Oxygen plasma etch is performed on a Unaxis Shuttlelock RIE/ICP reactive ion etcher. An Angstrom Engineering type-E CoVap electron beam evaporator is used to deposit metals. Optical reflection measurements are carried out using an Ocean Optics HR4000 high resolution fiber optic UV–vis spectrometer with reflection probes. Raman spectra are measured with a Renishaw inVia confocal Raman microscope.

Preparation of Gold-Coated Colloidal Crystal–Polymer Nanocomposites. The fabrication of wafer-scale, nonclosed-packed silica colloidal crystal–polymer nanocomposites is performed by following the established spin-coating procedures.³³ In short, Stöber silica colloids are first dispersed in an ETPTA monomer (with 2 wt % Darocur 1173 photoinitiator) to make a final particle volume fraction of 20%. The colloidal suspension is disposed on an APTCS-primed silicon wafer and spin-coated at 300 rpm for 1 min, 800 rpm for 1 min, 1500 rpm for 20 s, 3000 rpm for 20 s, and 7000 rpm for 2 min. The ETPTA monomer is rapidly polymerized for 12 s by using a pulsed UV curing system. Two nanometer chromium and 18 nm gold are finally deposited on the surface of the colloidal crystal–polymer nanocomposite by electron beam evaporation at a typical deposition rate of 0.1 nm/s from graphite crucibles at 2.5×10^{-6} mbar.

Normal Incidence Optical Reflection Measurements. A calibrated halogen light source is used to illuminate the sample. The beam spot size is about 3 mm on the sample surface. Measurements are performed at normal incidence, and the cone angle of collection is less than 5°. Absolute reflectivity is obtained as a ratio of the sample spectrum and reference spectrum. The reference spectrum is the optical density obtained from an aluminum-sputtered (1000 nm thickness) silicon wafer.

Raman Spectra Measurements. The gold-coated nanocomposites are immersed in a 5 mM solution of benzenethiol in 200 proof ethanol for 2 days and then dried in air for 20 min. Raman spectra are obtained using a 50× objective and a 785

nm diode laser at 0.5 mW with an integration time of 10 s and a 40 μm^2 spot size.

Electromagnetic Modeling of Raman Enhancement. In the finite-element method (FEM) model,³⁹ we suppose that the gold-coated nanocomposite is placed horizontally, so that the interface between the substrate and the medium (air) is parallel to the xz plane while the hemispherical protrusions are along the y axis. The total electromagnetic fields $E = E_{\text{inc}} + E_{\text{scatter}}$ and $H = H_{\text{inc}} + H_{\text{scatter}}$ should satisfy Maxwell's equations within medium and scatter (gold) domains

$$\begin{aligned}\nabla \times (\nabla \times E) - \omega^2 \epsilon \mu E &= 0 \\ \nabla \times (\nabla \times H) - \omega^2 \epsilon \mu H &= 0\end{aligned}\quad (1)$$

where ϵ and μ are domain-dependent permittivity and permeability, respectively, and ω is the light frequency. Continuity of tangential components of E and H across the interface between air and gold leads to the following boundary conditions with n as the interfacial normal vector

$$\begin{aligned}(E_1 - E_2) \times n &= 0 \\ (H_1 - H_2) \times n &= 0\end{aligned}\quad (2)$$

We then employ FEM under Comsol Multiphysics environment to solve eqs 1 and 2 for each substance (air and gold). Ten boundary layers around the medium and scatter domains are artificially constructed first. The “perfect matched layers” (PML) boundary approach is then used to define the boundary conditions for the bounded domains in order to obtain high-resolution numerical solutions.⁴⁰ The electronic and magnetic conductivity of each boundary layer can be set artificially so that little or no electromagnetic radiation will be reflected back into the domain of scatter. To simulate electromagnetic fields in the newly augmented domains, we solved Maxwell eq 1 in all subdomains. The boundary condition (eq 2) still holds for all internal interfaces. As to the outer boundaries of the PML layers, a low-reflection boundary condition (eq 3) is used to minimize residual reflection and attenuate the wave quickly within the layers

$$n \times (\nabla \times H_z) - j\omega H_z = 0 \quad (3)$$

After solving Maxwell eq 1 together with boundary conditions (eqs 2 and 3), the two-dimensional electric field can be used to calculate the order of magnitude of the Raman enhancement factor [$\log G(x, y)$] as⁴¹

$$\log G(x, y) = \log \left(\left| \frac{E(x, y)}{E_0} \right|^4 \right) \quad (4)$$

where $E(x, y)$ and E_0 are the electric field amplitude at location (x, y) and the incident field, respectively.

Results and Discussion

Contrary to traditional colloidal self-assembly technologies, which usually take days or even weeks to assemble centimeter-sized colloidal crystals as templates for making SERS substrates, the spin-coating technology is rapid and scalable. We have demonstrated that wafer-sized (up to 8 in. diameter) colloidal crystals can be fabricated in minutes.³³ In this methodology, monodispersed silica particles with diameter ranging from tens

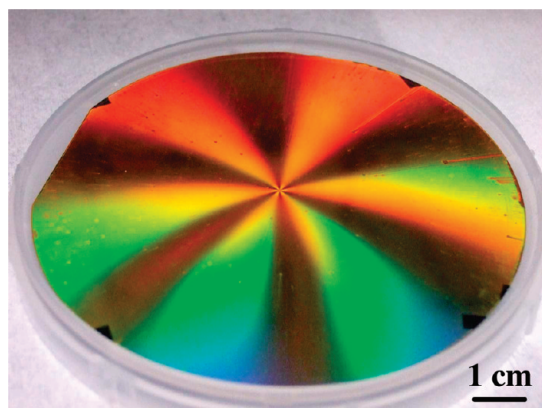


Figure 1. Photograph of a gold-coated colloidal crystal-polymer nanocomposite consisting of 320 nm silica spheres on a 4 in. silicon wafer illuminated with white light.

of nanometers to several micrometers are dispersed in a nonvolatile ETPTA monomer and then shear aligned to form highly ordered colloidal crystals by using standard spin-coating equipment.^{33,42} After photopolymerization of ETPTA monomers, the colloidal arrays are embedded in a polymer matrix, and the spheres of the top layer protrude out of the film, forming a periodic surface. The resulting colloidal crystal-polymer nanocomposites exhibit highly uniform thickness and remarkably large single-crystalline domain size over the whole wafer area. Another unique property of the shear-aligned colloidal crystal is the unusual nonclosed-packed structure.³³ The interparticle distance between neighboring colloids is fixed at ~ 1.4 times of the particle diameter.

The SERS-active substrate is fabricated by subsequent deposition of a 2 nm layer of chromium and an 18 nm layer of gold on the spin-coated nanocomposite by electron beam evaporation. Figure 1 shows a photograph of a metallized nanocomposite consisting of 320 nm silica spheres on a 4 in. silicon wafer illuminated with white light. The nanocomposite film is prepared by spin-coating a colloidal suspension at 7000 rpm for 2 min, having a thickness of 3 monolayers. The metallized sample exhibits a brilliant six arm diffraction star with exact 60° angles between neighboring arms. This pattern is caused by Bragg diffraction of visible light by the hexagonally ordered colloidal arrays.³³ Some defects (e.g., comets) caused by large airborne solid particles are apparent on the wafer. Many of these defects can be avoided by conducting spin-coating in a cleanroom.

Long-range hexagonal ordering and nonclosed-packing of the metallized colloidal crystal are evident in the typical top-view SEM image as shown in Figure 2A. Extensive SEM examination reveals that periodic colloidal arrays with similar crystalline structure and quality uniformly cover the whole wafer surface. Interestingly, the magnified SEM image in Figure 2B illustrates that the gold coating on the nanocomposite is rough, and gold islands of tens-of-nanometer-scale size and sub-10 nm gaps are clearly evident. The side-view SEM image in Figure 2C further confirms the granular microstructure of the deposited gold layer, and the protrusion depths of the spheres are measured to be ~ 80 nm.

Although island-type and discontinuous gold and silver films have been extensively studied for a wide range of applications such as molecular electronics and SERS,^{43–48} the formation of gold islands on the colloidal crystal-polymer nanocomposite is still somewhat unusual. As demonstrated in early studies, only when the metal film is thin (<10 nm nominal thickness for gold

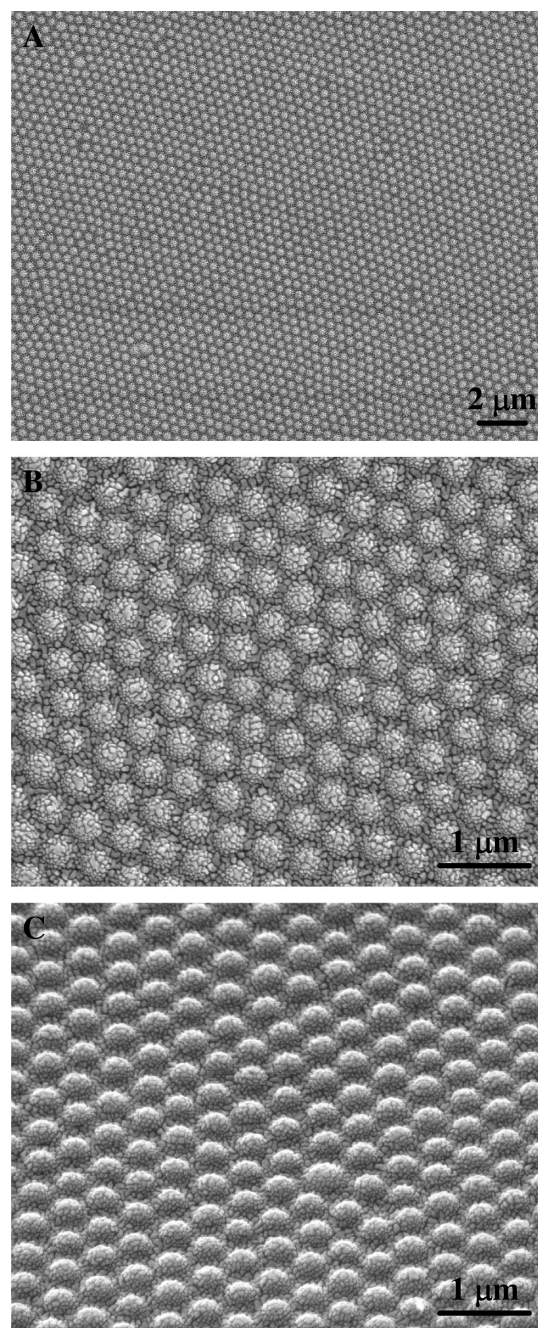


Figure 2. Scanning electron microscope (SEM) images of the gold-coated nanocomposite as shown in Figure 1. (A) Top view. (B) Magnified top view. (C) Tilted view (45°).

and <20 nm nominal thickness for silver), the surface condensation and nucleation of evaporated metal can induce the formation of island-type films.^{45,47,49} However, the thickness of the evaporated gold on the spin-coated nanocomposite is 18 nm, which is above the threshold for the formation of discontinuous films.⁴⁹ Control experiments show that evaporated gold of similar thickness forms continuous films on flat glass substrates. It is known that a thin (~ 80 nm) polymer wetting layer uniformly covers the protruded spheres of the spin-coated nanocomposite.³³ To evaluate the effect of this polymer layer on the formation of gold islands, we selectively remove the polymer layer on the protruded silica spheres by a brief oxygen plasma etch (40 mTorr oxygen pressure, 40 SCCM flow rate, and 100 W for 15, 30, and 45 s) and then deposit chromium and gold with similar thicknesses as the nanocomposite sample.

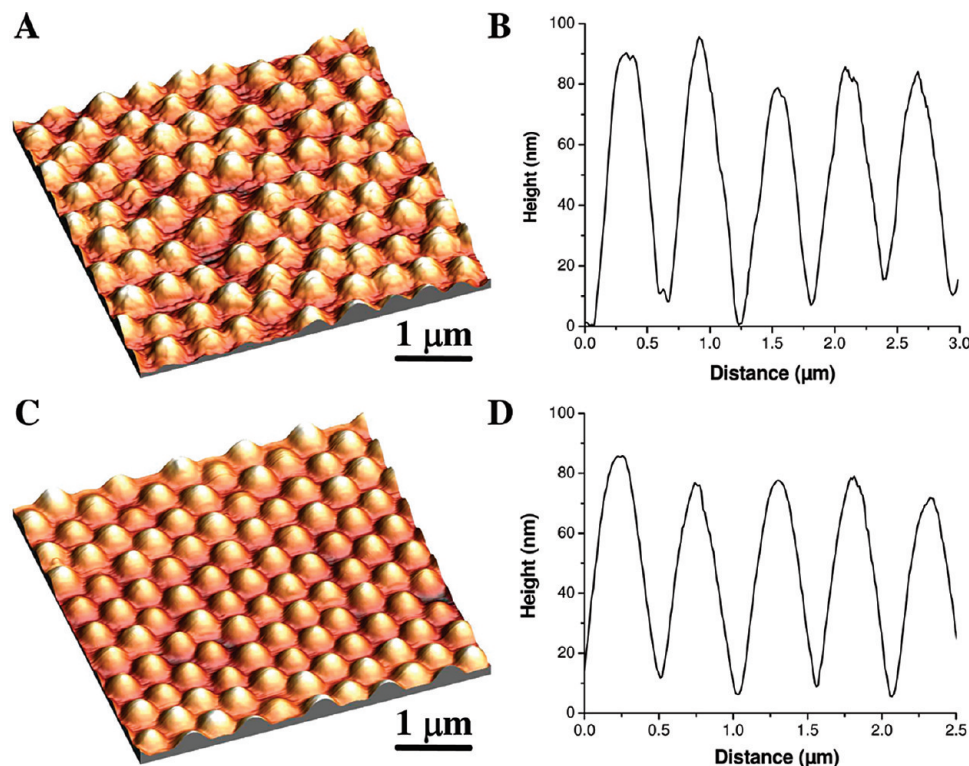


Figure 3. Tapping mode atomic force microscope (AFM) images and corresponding depth profiles. (A and B) Metallized nanocomposite consisting of 320 nm silica spheres. (C and D) Same sample after dissolving the metal coating.

AFM images show that the resulting metal films are continuous and smooth. This indicates that the polymer wetting layer plays a crucial role in the formation of gold islands during the evaporation of a metal film.

We have also compared the AFM images and corresponding depth profiles of the metallized nanocomposite and the same sample after wet-etching the gold and chromium layers in Figure 3. The metallized sample exhibits a rough and granular surface, and the root mean squared surface roughness (R_{rms}) is measured to be 3.48. After removing the metal coating, the nanocomposite surface is smooth, and the roughness is reduced to 1.05, which is almost identical to that of a newly spin-coated sample. This suggests that the formation of gold islands is not because of the surface buckling of the polymer nanocomposite caused by the deposition of metals. The depth profiles in panels B and D of Figure 3 show that the protrusion depths of the silica spheres retain after metal evaporation, indicating conformal deposition of metals on the surface of the nanocomposite. Although the underlying mechanism for the formation of gold islands during evaporation of relatively thick metals has yet to be fully understood and is still under investigation, the creation of discontinuous metal films with periodic microstructures over wafer-scale areas could find important technological applications in nanoelectronics, electromechanical devices (e.g., strain gauge), and biosensors.^{43–45}

Here, we focus on the application of these structured metal films as reproducible SERS substrates. Figure 4 compares the SER spectra of benzenethiol molecules adsorbed on a continuous gold control sample and a 18 nm gold-coated nanocomposite consisting of 400 nm silica spheres. Benzenethiol is chosen as the model molecule because of its ability to assemble into dense monolayers on gold and its large Raman cross section.²⁶ The periodic, island-type gold film shows strong and distinctive SERS peaks, whose positions and relative amplitude match with those in the literature for benzenethiol molecules adsorbed on

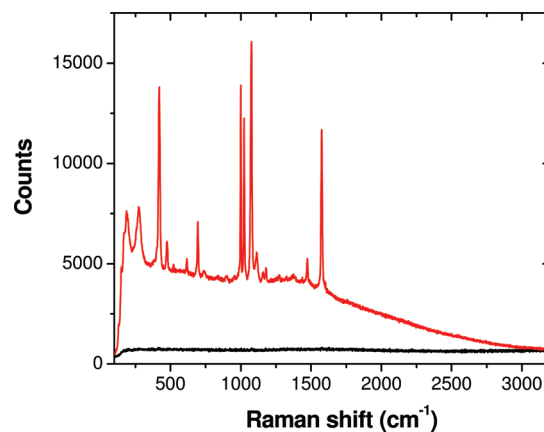


Figure 4. SER spectra obtained on a gold-coated nanocomposite consisting of 400 nm silica spheres (red) and a flat gold control sample on glass (black). The spectra were taken using a 785 nm diode laser at 0.5 mW with an integration time of 10 s.

structured gold surfaces,²⁶ while the flat gold control sample does not display clear SERS signal. The assignment of the SERS peaks to different vibrational modes is shown in Table 1. The SERS enhancement factor, G , is calculated using the method described in the literature by comparing the Raman intensity (after baseline subtraction) for various vibrational peaks obtained for a pure benzenethiol liquid (I_{bulk}) and at the metallized nanocomposite surface (I_{surf}) as⁹

$$G = \frac{C_{\infty} N_A \sigma h I_{\text{surf}}}{R I_{\text{bulk}}} \quad (5)$$

where C_{∞} is 9.8 M, N_A is Avogadro's number, σ is the gold surface area covered by benzenethiol molecules (0.45 nmol cm⁻²),²⁵ h is the confocal length of the spectrometer ($\sim 88 \mu\text{m}$

TABLE 1: Assignment of SERS Peaks and Corresponding Average Raman Counts^a

peak/(cm ⁻¹)	assignment	region	Raman counts	
			320 nm	400 nm
1575	a1, $\nu(\text{C}-\text{C}-\text{C})$	R0	3099 \pm 698 (22.5%)	7460 \pm 1799 (24.1%)
		R1	3606 \pm 862 (23.9%)	7060 \pm 1542 (21.8%)
		R2	3370 \pm 772 (22.9%)	5162 \pm 776 (15.0%)
		R3	4499 \pm 590 (13.1%)	5521 \pm 901 (16.3%)
		R4	4853 \pm 624 (12.9%)	4368 \pm 715 (16.4%)
1074	a1, $\nu(\text{C}-\text{C}-\text{C})$ and $\nu(\text{C}-\text{S})$	R0	5505 \pm 1208 (21.9%)	10850 \pm 704 (6.5%)
		R1	6424 \pm 1282 (20.0%)	11969 \pm 1863 (15.6%)
		R2	6841 \pm 1135 (16.6%)	8135 \pm 1414 (17.4%)
		R3	8170 \pm 999 (12.2%)	8280 \pm 1155 (13.9%)
		R4	8103 \pm 1241 (15.3%)	7489 \pm 971 (13.0%)
1023	a1, $\nu(\text{C}-\text{H})$	R0	3480 \pm 841 (24.2%)	7604 \pm 850 (11.2%)
		R1	4016 \pm 969 (24.1%)	7712 \pm 1261 (16.4%)
		R2	4270 \pm 811 (19.0%)	5123 \pm 1032 (20.1%)
		R3	4939 \pm 668 (13.5%)	5141 \pm 904 (17.6%)
		R4	4890 \pm 920 (18.8%)	4389 \pm 729 (16.6%)
1000	a1, $\nu(\text{C}-\text{C}-\text{C})$	R0	4100 \pm 1000 (24.4%)	9164 \pm 897 (9.8%)
		R1	4910 \pm 1177 (24.0%)	8801 \pm 1397 (15.9%)
		R2	5183 \pm 918 (17.7%)	6345 \pm 1123 (17.7%)
		R3	6222 \pm 774 (12.4%)	6381 \pm 1004 (15.7%)
		R4	7221 \pm 1136 (15.7%)	5409 \pm 792 (14.6%)
695	a1, $\nu(\text{C}-\text{C}-\text{C})$ and $\nu(\text{C}-\text{S})$	R0	1112 \pm 197 (17.7%)	2179 \pm 458 (21.0%)
		R1	1207 \pm 301 (24.9%)	2190 \pm 552 (25.2%)
		R2	1180 \pm 267 (22.6%)	1607 \pm 343 (21.3%)
		R3	1337 \pm 223 (16.7%)	1222 \pm 213 (17.4%)
		R4	1560 \pm 381 (24.4%)	1500 \pm 330 (22.0%)
419	a1, $\nu(\text{C}-\text{C}-\text{C})$ and $\nu(\text{C}-\text{S})$	R0	3970 \pm 1041 (26.2%)	8142 \pm 1815 (22.3%)
		R1	4972 \pm 970 (19.5%)	8067 \pm 1135 (14.1%)
		R2	5354 \pm 847 (15.8%)	5777 \pm 1312 (22.7%)
		R3	6076 \pm 1010 (16.6%)	3860 \pm 888 (23.0%)
		R4	5697 \pm 1286 (22.6%)	6356 \pm 749 (11.8%)

^a Peaks and Raman counts recorded for benzenethiol molecules adsorbed on five areas (R0–R4) of 4 in. nanocomposites consisting of 320 and 400 nm silica spheres.

determined for the 50 \times objective used in the experiment), and R is the surface roughness (~ 3.5 measured by AFM).

We have systematically investigated the reproducibility of SERS enhancement over 4 in. diameter samples consisting of 320 and 400 nm silica spheres. Four concentric rings with radii of 0.5, 1.6, 2.7, and 3.8 cm separate the 4 in. wafers into five regions designated as R0, R1, R2, R3, and R4, respectively. In each region, we have randomly obtained at least 10 SER spectra, and the average Raman counts and corresponding standard deviation for different SERS peaks are listed in Table 1. From the Table 1, it is evident that the SERS enhancement is reproducible from place to place within each region. We have also calculated the standard deviation of the averaged Raman counts for each vibrational mode across the 4 in. wafer. The results are 19.4% (1575 cm⁻¹), 16.2% (1074 cm⁻¹), 14.2% (1023 cm⁻¹), 22.0% (1000 cm⁻¹), 13.8% (695 cm⁻¹), and 15.5% (419 cm⁻¹) for the 320 nm sample and 22.1% (1575 cm⁻¹), 20.9% (1074 cm⁻¹), 25.9% (1023 cm⁻¹), 23.0% (1000 cm⁻¹), 24.7% (695 cm⁻¹), and 27.6% (419 cm⁻¹) for the 400 nm sample. We therefore conclude that the templated substrates exhibit high SERS reproducibility with less than 28% standard deviation over a 4 in. wafer surface.

From the SERS measurements, we have also found that the peak position for any specific vibrational mode is almost identical with less than 1 nm variation from place to place on the 320 and 400 nm samples. Therefore, we arithmetically average the SER spectra from the five regions of the two 4 in. samples and show the results in Figure 5. We have also calculated the SERS enhancement factors using the averaged Raman intensity for different peaks, and the results are listed in Table 2. Because of a high scattering background for pure

benzenethiol, the peaks at 1575 and 1074 cm⁻¹ are beyond the detection limit of the spectrometer. Therefore, we only list SERS enhancement factors for other four peaks in Table 2. It is apparent from Table 2 that a SERS enhancement factor on the order of 10⁷ can be achieved, and the 400 nm sample exhibits a slight higher enhancement. It is also interesting to notice that for 320 nm silica spheres the enhancement factor tends to increase from the center of the wafer (R0 region) to the edge (R4 region), while this trend is reversed for 400 nm silica spheres. We speculate that the crystalline parameters (e.g., interparticle separation, particle protrusion depth, and single-crystalline domain size) could be slightly different from center to edge due to the nonuniform shear stress during the spin-coating process.²⁵ It is well-known that SERS enhancement is sensitive to the structural parameters of the samples.²⁵

To help understand the enhancement mechanism, we have conducted optical reflection measurements at normal incidence and finite element electromagnetic modeling. It is well-known that localized (Mie scattering-based, surrounding metal nanoparticles)^{4,6,31} and delocalized (Bragg scattering-based, covering micrometer-scale areas)^{50,51} surface plasmons play important roles in determining the amplitude of SERS enhancement. Bartlett et al. have demonstrated that periodically structured metallic nanovoids prepared by electrochemical deposition exhibit strong and reproducible SERS enhancement, even though the metal films are not rough.^{25,26} They have also shown that greatest SERS enhancement occurs when surface plasmon resonances on structured metallic surfaces are present at the excitation wavelength and Raman scattered wavelength.^{25,26} Compared to other metal island SERS substrates,^{43–48} which typically only exhibit localized surface plasmon resonance, our

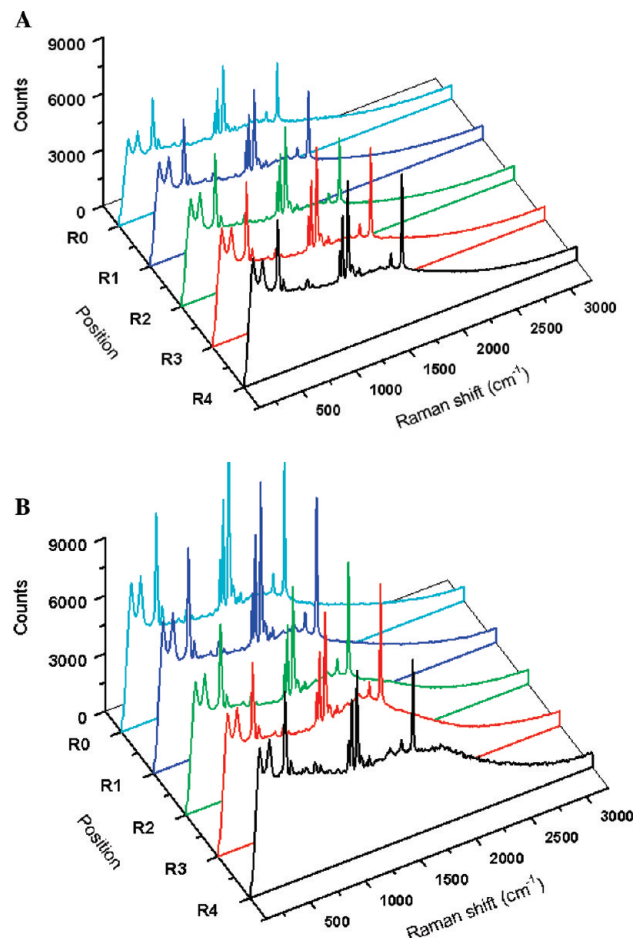


Figure 5. Arithmetically averaged SERS spectra recorded for benzenethiol molecules adsorbed on five areas (R0–R4) of 4 in. nanocomposites consisting of (A) 320 and (B) 400 nm silica spheres. Spectra were taken using a 785 nm diode laser at 0.5 mW with an integration time of 10 s.

TABLE 2: Assignment of SERS Peaks and Corresponding Raman Enhancement Factors^a

peak/(cm ⁻¹)	assignment	region	enhancement factor	
			320 nm	400 nm
1023	a ₁ , ν(C–H)	R0	2.2×10^7	4.8×10^7
		R1	2.6×10^7	4.9×10^7
		R2	2.7×10^7	3.3×10^7
		R3	3.2×10^7	3.3×10^7
		R4	3.1×10^7	2.8×10^7
1000	a ₁ , ν(C–C–C)	R0	6.5×10^6	1.5×10^7
		R1	7.8×10^6	1.4×10^7
		R2	8.2×10^6	1.0×10^7
		R3	9.8×10^6	1.0×10^7
		R4	1.1×10^7	8.6×10^6
695	a ₁ , ν(C–C–C) and ν(C–S)	R0	1.1×10^7	2.1×10^7
		R1	1.2×10^7	2.1×10^7
		R2	1.1×10^7	1.5×10^7
		R3	1.3×10^7	1.2×10^7
		R4	1.5×10^7	1.4×10^7
419	a ₁ , ν(C–C–C) and ν(C–S)	R0	4.9×10^7	1.0×10^8
		R1	6.2×10^7	1.0×10^8
		R2	6.6×10^7	7.2×10^7
		R3	7.5×10^7	4.8×10^7
		R4	7.1×10^7	7.9×10^7

^a Peaks and Raman enhancement factors were calculated for benzenethiol molecules adsorbed on five areas (R0–R4) of 4 in. nanocomposites consisting of 320 and 400 nm silica spheres.

periodic metal films could support localized and delocalized surface plasmons. The former is originated from the metal islands, while the latter is caused by the Bragg scattering from

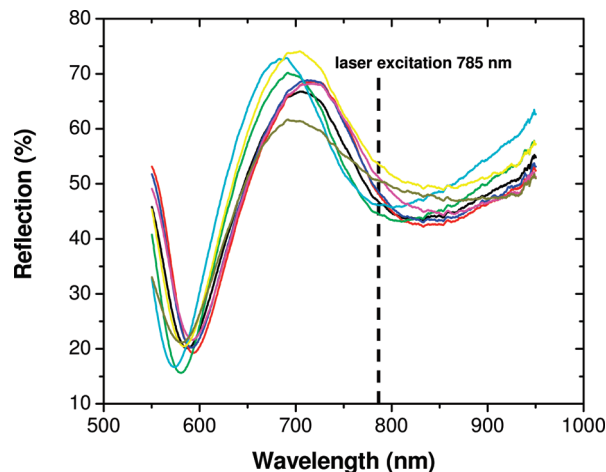


Figure 6. Normal incidence reflection spectra obtained at eight locations on a 4 in. metallized nanocomposite consisting of 400 nm silica spheres.

the periodic structure whose lattice constant matches with the wavelength of operating light. To evaluate the surface plasmon resonance of metallized nanocomposites, we measured optical reflection at normal incidence. Figure 6 shows the reflection spectra obtained at eight random locations on a metallized nanocomposite consisting of 400 nm silica spheres. The position of the laser excitation wavelength, 785 nm, is also indicated by the dashed line. The absorbance valleys (peaked at ~600 and 800 nm) in the reflection spectra could be attributed to the interference of the incident light with delocalized and localized surface plasmons as well as the colloidal multilayers.⁵⁰ It is evident that the position of the excitation laser almost coincides with the absorbance valley located at ~800 nm. This could result in high SERS enhancement as shown in Figure 5B.

To further evaluate the contribution of the delocalized surface plasmons to the overall SERS enhancement, we calculated the electric field amplitude distribution and corresponding Raman enhancement factors surrounding arrays of gold hemispherical protrusions using the Comsol Multiphysics software.³⁹ Because the periodic array is symmetric, we construct a simplified two-dimensional model which can be considered as sections through a three-dimensional array at the point of maximal enhancement (Figure 7A). Figure 7A shows the calculated distribution of a SERS enhancement factor around two adjacent hemispherical protrusions with a templating sphere diameter of 320 nm and interprotrusion distance of 1.4×320 nm. The simulation results show that the maximal SERS enhancement factors occur at the top of the semicircles. The spatial distribution of the enhancement factors around the two semicircles is asymmetric, indicating strong electromagnetic interaction between the neighboring scatters. Figure 7B illustrates that a larger array (12 semicircles) results in higher enhancement ($\sim 10^{4.6}$), and Figure 7C demonstrates that the maximal enhancement factor reaches a plateau when the array has more than 12 scatters. In real SERS experiments, the laser spot ($\sim 40 \mu\text{m}^2$) covers ~ 250 protrusions. It should be noted that the current electromagnetic modeling represents a significant simplification of the real case as the contributions from the localized surface plasmons caused by isolated gold islands and the charge transfer mechanism, which arises from the electronic interaction between the adsorbed molecules and metal surface,⁵² are not being considered. This could explain the large discrepancy between the experimental and calculated SERS enhancement. Indeed, the continuous and smooth gold films deposited on

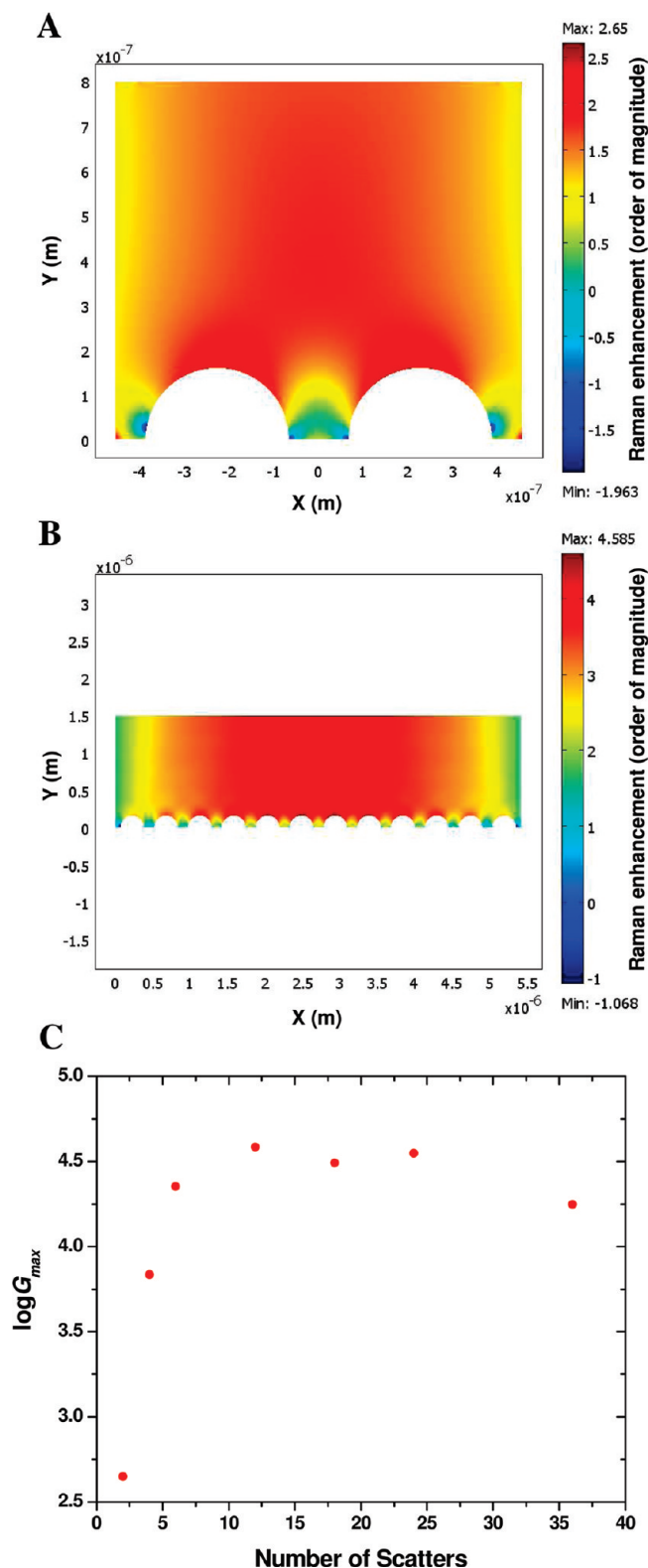


Figure 7. Simulated Raman enhancement around gold semispherical protrusions templated from 320 nm silica spheres at $\lambda = 785$ nm. (A) 2 scatterers. (B) 12 scatterers. (C) Simulated order of magnitude of maximal SERS enhancement factor ($\log G_{\max}$) versus number of scatterers.

the oxygen plasma-etched nanocomposites exhibit a much lower SERS enhancement factor ($<10^5$) than that of the discontinuous films as shown in Figure 5.

Conclusions

In conclusion, we have developed a simple and scalable bottom-up approach for fabricating periodically structured

surfaces that can serve as substrates for depositing gold island films with reproducible SERS enhancement over wafer-sized areas. The technology only requires a single metal deposition step to create the resulting SERS-active substrates on a self-assembled colloidal template. It leverages the demonstrated uniformity of spin-coated colloidal arrays and conventional physical vapor deposition techniques. The formation of discontinuous, island-type metal films with periodic microstructures over large areas could lead to important technological applications in nanoelectronics, electromechanical devices, and biosensors.

Acknowledgment. This work was supported in part by National Science Foundation Grants CBET-0651780 and CBET-0744879, start-up funds from the University of Florida, and the UF Research Opportunity Incentive Seed Fund. X.F.L. acknowledges the China Scholarship Council for financial support.

References and Notes

- (1) Baker, G. A.; Moore, D. S. *Anal. Bioanal. Chem.* **2005**, *382*, 1751.
- (2) Dieringer, J. A.; McFarland, A. D.; Shah, N. C.; Stuart, D. A.; Whitney, A. V.; Yonzon, C. R.; Young, M. A.; Zhang, X. Y.; Van Duyne, R. P. *Faraday Discuss.* **2006**, *132*, 9.
- (3) Haynes, C. L.; Yonzon, C. R.; Zhang, X. Y.; Van Duyne, R. P. *J. Raman Spectrosc.* **2005**, *36*, 471.
- (4) Kneipp, K.; Kneipp, H.; Kneipp, J. *Acc. Chem. Res.* **2006**, *39*, 443.
- (5) Le Ru, E. C.; Etchegoin, P. G. *Principles of Surface Enhanced Raman Spectroscopy and Related Plasmonic Effects*; Elsevier: Amsterdam, 2009.
- (6) Aroca, R. *Surface-Enhanced Vibrational Spectroscopy*; John Wiley & Sons: Chichester, U.K., 2006.
- (7) Freeman, R. G.; Grabar, K. C.; Allison, K. J.; Bright, R. M.; Davis, J. A.; Guthrie, A. P.; Hommer, M. B.; Jackson, M. A.; Smith, P. C.; Walter, D. G.; Natan, M. J. *Science* **1995**, *267*, 1629.
- (8) Chattopadhyay, S.; Chen, L. C.; Chen, K. H. *Crit. Rev. Solid State Mater. Sci.* **2006**, *31*, 15.
- (9) Tian, Z. Q.; Ren, B.; Wu, D. Y. *J. Phys. Chem. B* **2002**, *106*, 9463.
- (10) Roca, M.; Haes, A. J. *J. Am. Chem. Soc.* **2008**, *130*, 14273.
- (11) Braun, G.; Pavel, I.; Morrill, A. R.; Seferos, D. S.; Bazan, G. C.; Reich, N. O.; Moskovits, M. J. *Am. Chem. Soc.* **2007**, *129*, 7760.
- (12) McLellan, J. M.; Li, Z. Y.; Siekkinen, A. R.; Xia, Y. N. *Nano Lett.* **2007**, *7*, 1013.
- (13) Wang, H.; Levin, C. S.; Halas, N. J. *J. Am. Chem. Soc.* **2005**, *127*, 14992.
- (14) Jackson, J. B.; Halas, N. J. *Proc. Natl. Acad. Sci. U.S.A.* **2004**, *101*, 17930.
- (15) Nie, S. M.; Emery, S. R. *Science* **1997**, *275*, 1102.
- (16) Qian, X. M.; Nie, S. M. *Chem. Soc. Rev.* **2008**, *37*, 912.
- (17) Le Ru, E. C.; Blackie, E.; Meyer, M.; Etchegoin, P. G. *J. Phys. Chem. C* **2007**, *111*, 13794.
- (18) Fleischmann, M.; Hendra, P. J.; McQuillan, A. J. *Chem. Phys. Lett.* **1974**, *26*, 163.
- (19) Chang, H.; Hwang, K. C. *J. Am. Chem. Soc.* **1984**, *106*, 6586.
- (20) Jeanmaire, D. L.; Van Duyne, R. P. *J. Electroanal. Chem.* **1977**, *84*, 1.
- (21) Kudelski, A.; Bukowska, J. *Vib. Spectrosc.* **1996**, *10*, 335.
- (22) Stolberg, L.; Lipkowski, J.; Irish, D. E. *J. Electroanal. Chem.* **1991**, *300*, 563.
- (23) Kahl, M.; Voges, E.; Kostrewa, S.; Viets, C.; Hill, W. *Sens. Actuators, A* **1998**, *51*, 285.
- (24) Oran, J. M.; Hinde, R. J.; Abu Hatab, N.; Retterer, S. T.; Sepaniak, M. J. *J. Raman Spectrosc.* **2008**, *39*, 1811.
- (25) Abdelsalam, M. E.; Mahajan, S.; Bartlett, P. N.; Baumberg, J. J.; Russell, A. E. *J. Am. Chem. Soc.* **2007**, *129*, 7399.
- (26) Cintra, S.; Abdelsalam, M. E.; Bartlett, P. N.; Baumberg, J. J.; Kelf, T. A.; Sugawara, Y.; Russell, A. E. *Faraday Discuss.* **2006**, *132*, 191.
- (27) Dick, L. A.; McFarland, A. D.; Haynes, C. L.; Van Duyne, R. P. *J. Phys. Chem. B* **2002**, *106*, 853.
- (28) Tessier, P. M.; Velez, O. D.; Kalambur, A. T.; Rabolt, J. F.; Lenhoff, A. M.; Kaler, E. W. *J. Am. Chem. Soc.* **2000**, *122*, 9554.
- (29) Zhang, X. Y.; Young, M. A.; Lyandres, O.; Van Duyne, R. P. *J. Am. Chem. Soc.* **2005**, *127*, 4484.
- (30) Jang, S. G.; Choi, D. G.; Heo, C. J.; Lee, S. Y.; Yang, S. M. *Adv. Mater.* **2008**, *20*, 4862.
- (31) Haynes, C. L.; Van Duyne, R. P. *J. Phys. Chem. B* **2001**, *105*, 5599.
- (32) Fang, Y.; Seong, N. H.; Dlott, D. D. *Science* **2008**, *321*, 388.

- (33) Jiang, P.; McFarland, M. J. *J. Am. Chem. Soc.* **2004**, *126*, 13778.
- (34) Jiang, P.; Prasad, T.; McFarland, M. J.; Colvin, V. L. *Appl. Phys. Lett.* **2006**, *89*, 011908.
- (35) Sun, C. H.; Linn, N. C.; Jiang, P. *Chem. Mater.* **2007**, *19*, 4551.
- (36) Lin, T. H.; Linn, N. C.; Tarajano, L.; Jiang, B.; Jiang, P. *J. Phys. Chem. C* **2009**, *113*, 1367.
- (37) Linn, N. C.; Sun, C. H.; Arya, A.; Jiang, P.; Jiang, B. *Nanotechnology* **2009**, *20*, 225303.
- (38) Stober, W.; Fink, A.; Bohn, E. *J. Colloid Interface Sci.* **1968**, *26*, 62.
- (39) Brown, R. J. C.; Wang, J.; Tantra, R.; Yardley, R. E.; Milton, M. J. T. *Faraday Discuss.* **2006**, *132*, 201.
- (40) Jin, J. *The Finite Element Method in Electromagnetics*, 2nd, ed.; John Wiley and Sons: New York, 2002.
- (41) Moskovits, M. *Rev. Mod. Phys.* **1985**, *57*, 783.
- (42) Min, W. L.; Jiang, P.; Jiang, B. *Nanotechnology* **2008**, *19*, 475604.
- (43) Wei, H. Y.; Eilers, H. *J. Phys. Chem. Solid* **2009**, *70*, 459.
- (44) Bendikov, T. A.; Rabinkov, A.; Karakouz, T.; Vaskevich, A.; Rubinstein, I. *Anal. Chem.* **2008**, *80*, 7487.
- (45) Seminario, J. M.; Ma, Y. F.; Agapito, L. A.; Yan, L. M.; Araujo, R. A.; Bingi, S.; Vadlamani, N. S.; Chagarlamudi, K.; Sudarshan, T. S.; Myrick, M. L.; Colavita, P. E.; Franzon, P. D.; Nackashi, D. P.; Cheng, L.; Yao, Y. X.; Tour, J. M. *J. Nanosci. Nanotech.* **2004**, *4*, 907.
- (46) Semin, D. J.; Rowlen, K. L. *Anal. Chem.* **1994**, *66*, 4324.
- (47) Vanduyne, R. P.; Hulteen, J. C.; Treichel, D. A. *J. Chem. Phys.* **1993**, *99*, 2101.
- (48) Schlegel, V. L.; Cotton, T. M. *Anal. Chem.* **1991**, *63*, 241.
- (49) Maissel, L. I.; Glang, R. *Handbook of Thin Film Technology*; McGraw-Hill: New York, 1970.
- (50) Kelf, T. A.; Sugawara, Y.; Cole, R. M.; Baumberg, J. J.; Abdelsalam, M. E.; Cintra, S.; Mahajan, S.; Russell, A. E.; Bartlett, P. N. *Phys. Rev. B* **2006**, *74*, 245415.
- (51) Sugawara, Y.; Kelf, T. A.; Baumberg, J. J.; Abdelsalam, M. E.; Bartlett, P. N. *Phys. Rev. Lett.* **2006**, *97*, 266808.
- (52) Campion, A.; Ivanecky, J. E.; Child, C. M.; Foster, M. *J. Am. Chem. Soc.* **1995**, *117*, 11807.

JP905065Z